Spinup of a Submesoscale Eddy in the TOGA COARE Intensive Flux Array during the Spindown of an Intense Eastward Jet*

MING FENG,+ ROGER LUKAS, AND PETER HACKER

School of Ocean and Earth Science and Technology, University of Hawaii, Honolulu, Hawaii

(Manuscript received 19 October 1999, in final form 12 May 2000)

ABSTRACT

During the TOGA COARE Intensive Observing Period, an energetic, surface-intensified, submesoscale cyclonic eddy was observed in the near-equatorial western Pacific warm pool. The eddy appeared to have been generated as part of the spindown of a strong eastward surface jet forced by the December 1992 westerly wind burst. Because of its potential impacts on the long-term heat, salt, and momentum budgets of the warm pool, the authors provide a thorough description of the evolution of the surface jet and the development of the eddy in the present study. Both the isopycnal surface fit and the zeroth-order dynamic balance confirm the existence of the eddy. Surface layer convergence and northward inertial motion are suggested to be the main causes of the negative eddy vorticity, and it is likely that the eddy drew its energy from the decaying surface jet. This study indicates that in the near-equatorial region the inertial motion has a decreasing meridional spatial scale with time, $(\beta t)^{-1}$, due to the β effect, which increases the Rossby number of the decaying jet and generates the nonlinearity.

1. Introduction

During the Intensive Observing Period (IOP) of the Tropical Ocean Global Atmosphere Coupled Ocean–Atmosphere Response Experiment (TOGA COARE: Webster and Lukas 1992), an intense, jetlike eastward current was spun up in the upper 70 m of the ocean by a strong westerly wind burst (WWB) event in late December 1992 to early January 1993. Maximum observed current speed was about 1 m s^{-1} near the equator (Eldin et al. 1994; Ralph et al. 1997), comparable to previously observed upper-ocean response to the WWBs. This eastward jet extended well south of the equator; peak eastward flow was about 0.6 m s^{-1} in the Intensive Flux Array (IFA) centered near 2°S, 156°E (Smyth et al. 1996; Feng et al. 1998b). When the winds calmed, the jet began to rapidly spin down. Part of this process was the generation of an energetic, surface-intensified, cyclonic eddy along the southern flank of the jet, nearly centered in the IFA, which was captured by a repeated survey during the IOP (Lukas et al. 1995). The eddy radius was about 50 km, smaller than the Rossby radius of deformation, so that it is in the category of submesoscale.

That the eddy was associated with the decay of the equatorial jet suggests that nonlinear dynamics may be important for modeling the local momentum balance of the decay process, which has been overlooked by linear theories (Philander 1978; Eriksen 1993). This scale of motion is usually not resolved by general circulation models, some of which are used to predict the temporal response pattern of such jets for ENSO forecasting.

In the present study, we present a thorough description of the evolution of the jet and the development of the eddy in section 3, after first describing the observational methods in section 2. In section 4, we fit a Gaussian shape to the isopycnal data to determine the spatial scale of the variability. In section 5, we explore the dynamics of the eddy, and in section 6, we briefly discuss and summarize the results.

2. Data

During the IOP, the R/V *Wecoma* repeatedly surveyed the upper ocean in the IFA along a butterfly pattern centered at 1.8°S, 156.1°E (Fig. 1). The survey extended over 130 km in both zonal and meridional directions and was repeated approximately every 36 hours. Three survey cruises were conducted between early November

* School of Ocean and Earth Science and Technology Contribution Number 5284 and International Pacific Research Center Publication Number 62.

+ Current affiliation: Division of Marine Research, CSIRO, Hobart, Tasmania, Australia.

Corresponding author address: Dr. Roger Lukas, Department of Oceanography, University of Hawaii at Manoa, 1000 Pope Road, Honolulu, HI 96822.
E-mail: rlukas@soest.hawaii.edu

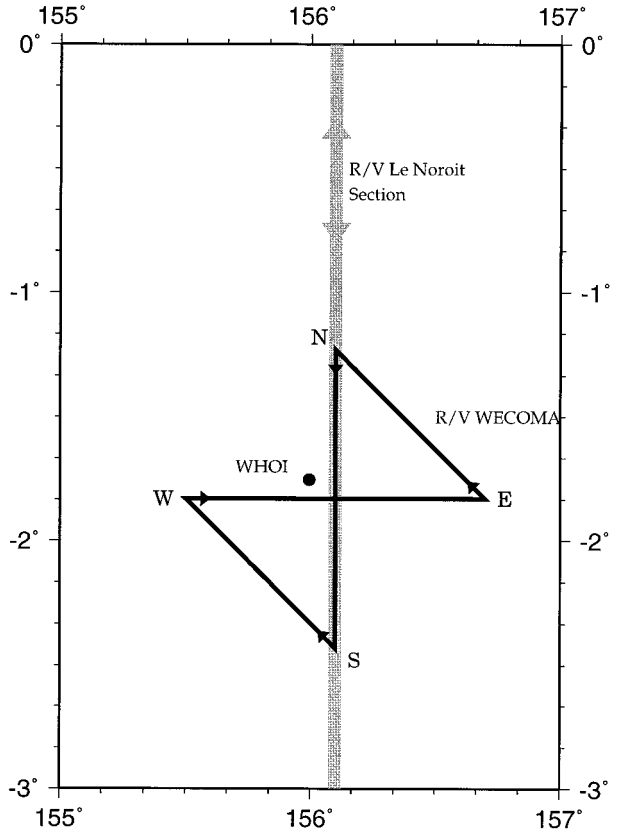

FIG. 1. Map of the R/V *Wecoma* and R/V *Le Noroit* sampling tracks in the IFA during Cruise 2 of the COARE IOP. Sections along the *Wecoma* track are later referred to by the connected apexes (labeled), such as north-to-south (N2S), etc. Location of the WHOI mooring is indicated.

1992 and late February 1993 (Huyer et al. 1997; Feng et al. 2000), the data used for the present study are from the second cruise. Nearly continuous acoustic Doppler current profiler (ADCP) and Seasoar/conductivity–temperature–depth (CTD) temperature and salinity measurements were made along the ship track. Hourly averaged data are used for the present study, with a horizontal resolution of about 15 km. Barotropic and a deterministic fraction of the baroclinic semidiurnal tides are eliminated using a simple linear plane-wave model (Feng et al. 1998a). Soloviev et al. (2000) confirm the tidal model using wavenumber spectrum analysis.

Air–sea flux observations were made aboard the R/V *Wecoma* and at a central surface mooring (deployed by Woods Hole Oceanographic Institution, hereafter called the WHOI mooring) during the IOP (Weller and Anderson 1996). The WHOI mooring was located at 1°45°S, 156°E, near the center of the *Wecoma* butterfly survey pattern (Fig. 1); hourly surface wind and upper-ocean velocity data during the IOP are used. A Doodson filter (Schureman 1958) is used to remove the tidal signal in the WHOI mooring velocity data. The wind stress curl is calculated using National Centers for Environmental Prediction reanalysis data.

The R/V *Le Noroit* repeatedly occupied a section along 156.1°E between 5°S and 5°N during the IOP (Eldin et al. 1994). Temperature, salinity, and velocity were measured along the ship track with Seasoar/CTD and ADCP. Data from one north-to-south *Le Noroit* section that crossed the IFA on 8 January 1993 are used in the present study.

3. Eddy description

During cruise 2 of the IOP survey (19 Dec 1992–10 Jan 1993), there was a multipeak WWB event, with the last westerly wind peak occurring from 29 December 1992 to 2 January 1993 (Weller and Anderson 1996; Smyth et al. 1996; Feng et al. 1998b). Figure 2 shows the hourly wind speed and direction, and detided current velocity in the upper 100 m at the WHOI mooring during 29 December through 11 January. The WWB wind was toward the southeast with peak value of more than 9 m s^{-1}, and it started to weaken rapidly from 1200 UTC 2 January. After 3 January, the wind speed was mostly less than 4 m s^{-1}.

The initial southeastward flow of more than 0.1 m s^{-1} on 29 December was due to earlier westerly peaks (Smyth et al. 1996). The eastward surface jet during the present westerly period had peak eastward flow of about 0.6 m s^{-1} at the WHOI mooring site on 3 January (Figs. 2 and 3a). There was also a subsurface countercurrent in phase with the surface peak (Huyer et al. 1997; Zhang and Rothstein 1998; Richardson et al. 1999). Starting from 3 January, the eastward jet lost strength and began to turn northward due to inertial effects. The local inertial period at the WHOI mooring site is 16 days. The peak northward current of 0.4 m s^{-1} was reached at 32-m depth on 7 January. After that, instead of rotating counterclockwise/anticyclonically, the surface current was accelerated toward the east during 7–9 January, apparently not forced by the local surface wind. We believe that this was due to the presence of a cyclonic eddy centered south of the WHOI mooring, which spun up when the eastward surface jet decayed (Lukas et al. 1995).

The *Wecoma* 20–50-m mean current velocity (Fig. 3) provides a clearer record of the cyclonic eddy spinup process. The mean velocity from the WHOI mooring during different intervals agrees well with the current structure in the *Wecoma* data. When the westerly winds started to decrease during 2 January to the middle of 3 January, the eastward jet attained its full strength with peak velocity of 0.6 m s^{-1} (Fig. 3a). On 2 January, the surface jet had two branches, separated at 2°S by a minimum of zonal current, and the meridional velocity component was small (Fig. 4a). There was a westward subsurface countercurrent immediately below 80 m, so that the vertical shear of the zonal current was large. From the potential density data, strong stratification of the

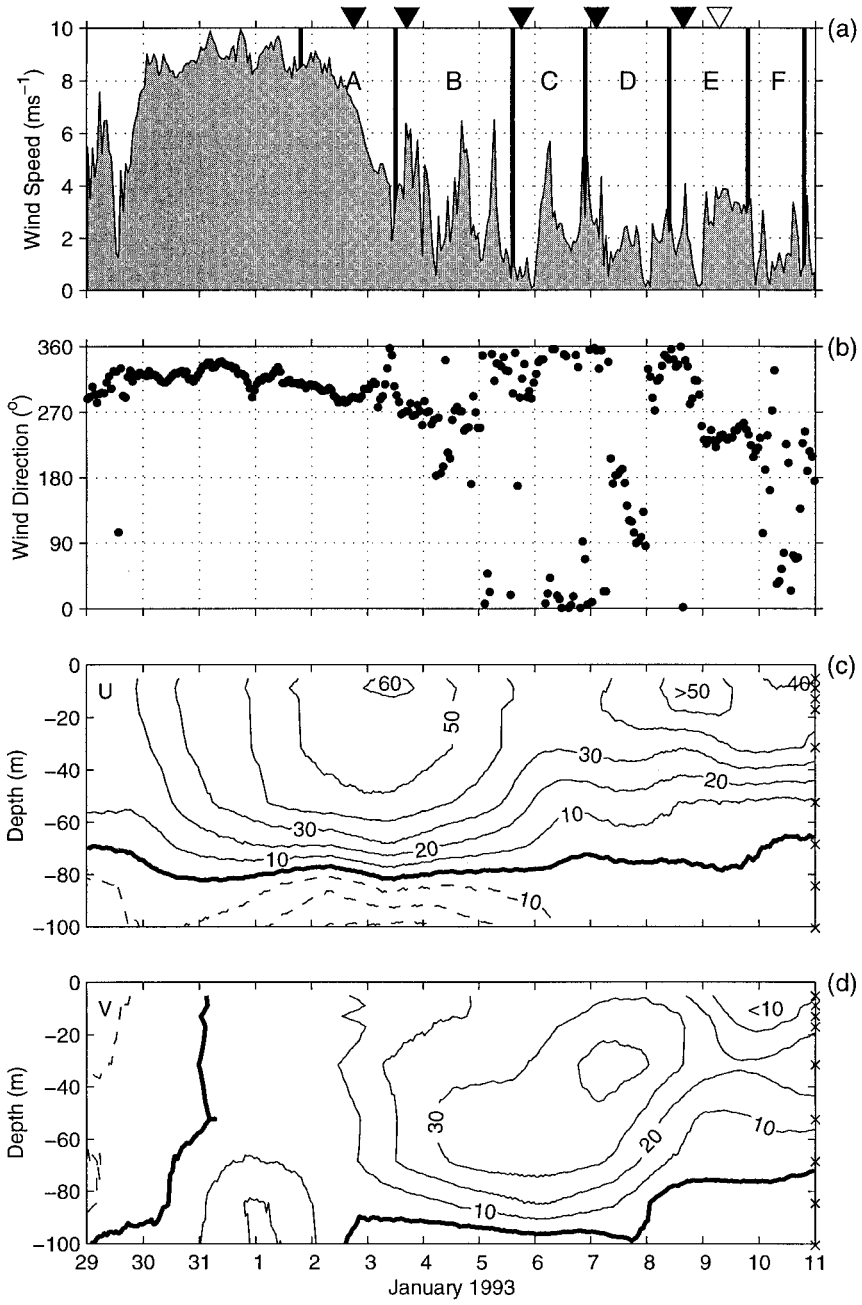

FIG. 2. (a) Wind speed, (b) wind direction, (c) eastward, and (d) northward current velocity components (cm s^{-1}) in the upper 100 m from the WHOI mooring during 29 Dec–11 Jan. The heavy vertical lines denote the segments for the six time intervals used in Fig. 3. The black triangles denote the center time for the N2S meridional sections described in Fig. 4, and the white triangle denotes the center time for the W2E section on 9 Jan described in Fig. 5. Negative velocities in (c) and (d) are denoted with dashed contours. The crosses on the right-hand side axes in (c) and (d) denote the depths of current measurements.

seasonal thermocline started from about 80 m and a weak frontlike feature developed above 70 m (Fig. 4a).

From the middle of 3 January, the jet began to rapidly spin down and near-inertial motions were generated. The inertial period varies from 23 days at the northern apex of the butterfly pattern to 12 days at the southern apex so that the spindown of the strong eastward jet was strongly shaped by the β effect. From the middle of January 3 to 6 January, the current weakened and rotated counterclockwise (Fig. 3b and 3c). From the

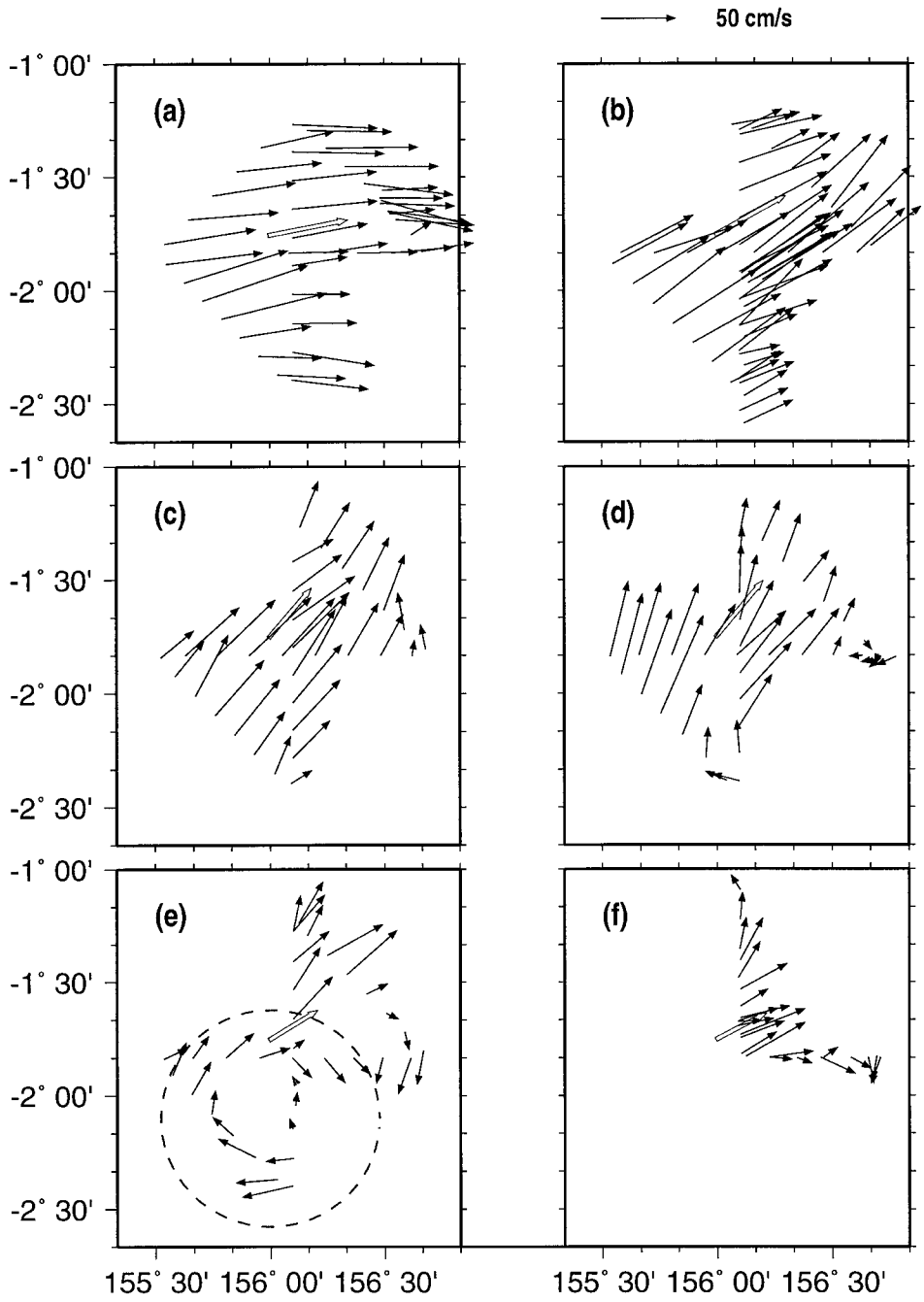

FIG. 3. Maps of 20–50-m averaged velocity along the *Wecoma* track during the six time periods denoted in Fig. 2. The white arrows denote the WHOI mean velocity during the same time periods. The dashed circle in (e) denotes the location and *e*-folding radius of the eddy determined from the Gaussian fit.

N2S section on 3 January (Fig. 4b), the eastward component of the jet was slightly stronger than on 2 January, and with a broader northern branch and a smaller southern branch. A northward component existed in the surface layer; southward motion existed below 80 m in the southern portion of the survey, which might be due to the inertial relaxation of the subsurface countercurrent. On 5 January (Fig. 4c), the zonal components of the surface current and the subsurface countercurrent were both weakened. The meridional component in the surface layer had strengthened and its peak extended downward toward the equator, which is consistent with the near-inertial wave energy propagation (Eriksen 1999), although the partition between the surface-trapped en-

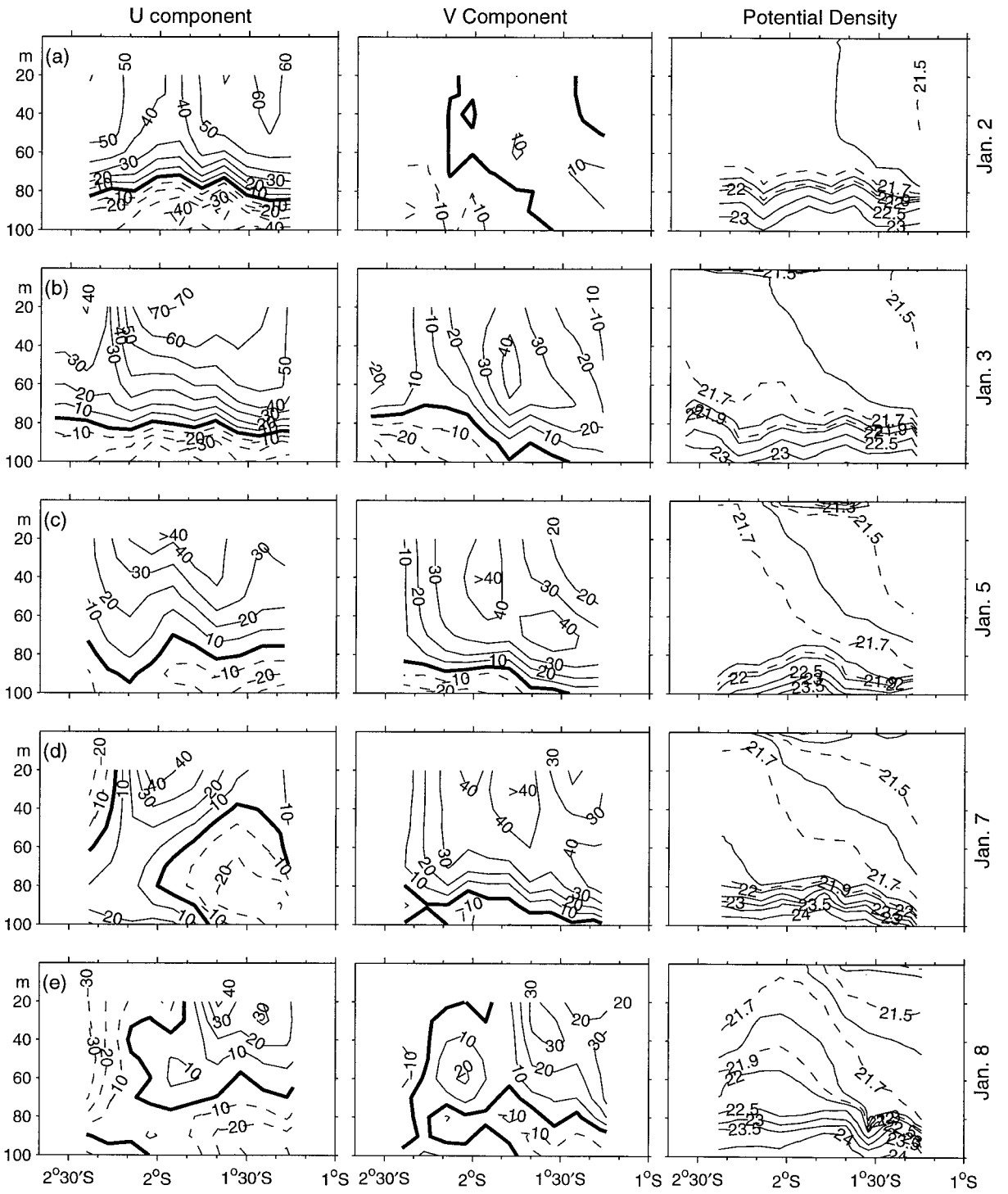

FIG. 4. Zonal and meridional current speeds (cm s^{-1}) and potential density from the five N2S *Wecoma* sections at the times denoted by the solid triangles in Fig. 2. Negative velocities (westward and southward) are denoted by dashed contours. In the density plots, the isopycnals above 22 σ_θ have 0.1 kg m^{-3} interval, and 0.5 below.

ergy and vertically propagating energy still needs to be addressed. Some small-scale variability in the inertial motion might be due to the inhomogeneity of the wind-driven jet.

On 7 January, the current velocity over most of the area pointed toward the north or northeast, while the current at the southern apex had rotated to nearly westward (Fig. 3d). The eastward jet had broken down and there was only a narrow remnant near 2°S, while westward zonal velocity appeared south of it (Fig. 4d). The meridional component was slightly strengthened. The strength of the meridional density gradient had increased with the decay of the surface jet (Figs. 4b–d) and the 21.7 σ_θ isopycnal was as deep as 80 m at the northern apex, but almost surfaced near the southern apex during 5–7 January (Figs. 4c and 4d). Feng et al. (1998b) found that the combination of the inertial motion and the meridional frontal structure greatly influenced the upper-ocean heat/salt budget through meridional advection.

By 8 January, the cyclonic eddy had spun up in the southern flank of the survey, centered south-southwest of the butterfly crossover point (Fig. 3e). The northern limb of the eddy had moved slightly eastward about two days later on 10 January (Fig. 3f). Unfortunately, we could not observe the evolution of the eddy beyond this point. The radius of the eddy is about 50 km (corresponding to the horizontal length scale of the eddy L), and a typical velocity associated with the eddy is 0.4 m s^{-1} (corresponding to the horizontal velocity scale of the eddy U). Thus, the Rossby number Ro $= U/f_0L$ is about 1.6 ($f_0 = -5 \times 10^{-6}$ s^{-1} at 2°S), indicating that the nonlinear term is more important than the Coriolis term in the dynamic balance of the eddy. From the zonal current structure, the eddy was shallow in the north and deeper than 90 m in the south, centered near 2°S (Fig. 4e). The southern limb was not fully covered by the survey. Near the northern apex of the survey, the current was toward the northeast at this time, which might be influenced by the remnant of the inertial motion. Near the center of the eddy, the current velocity was typically less than 0.1 m s^{-1}. When the eddy was fully developed, the 21.7 kg m^{-3} isopycnal had a domed structure with peak shallower than 10 m depth centered at 2°S, south of the crossover point of the butterfly pattern (Fig. 4e). It was still as deep as 80 m at the northern apex. The domed structure in the 21.9–22 kg m^{-3} isopycnals shifted slightly to the south with increasing depth. North of the domed structure, the weak meridional gradient still existed.

Figure 5 shows a zonal section on 9 January after the eddy developed. This west-to-east (W2E) section cut through the northern portion of the eddy; thus the flow was toward the northeast on the western flank, while largely toward the southeast on the eastern flank. The isopycnals between 21.6 and 22 σ_θ also had a domed structure. This further confirms that an eddy had developed instead of a zonally elongated north–south frontal structure.

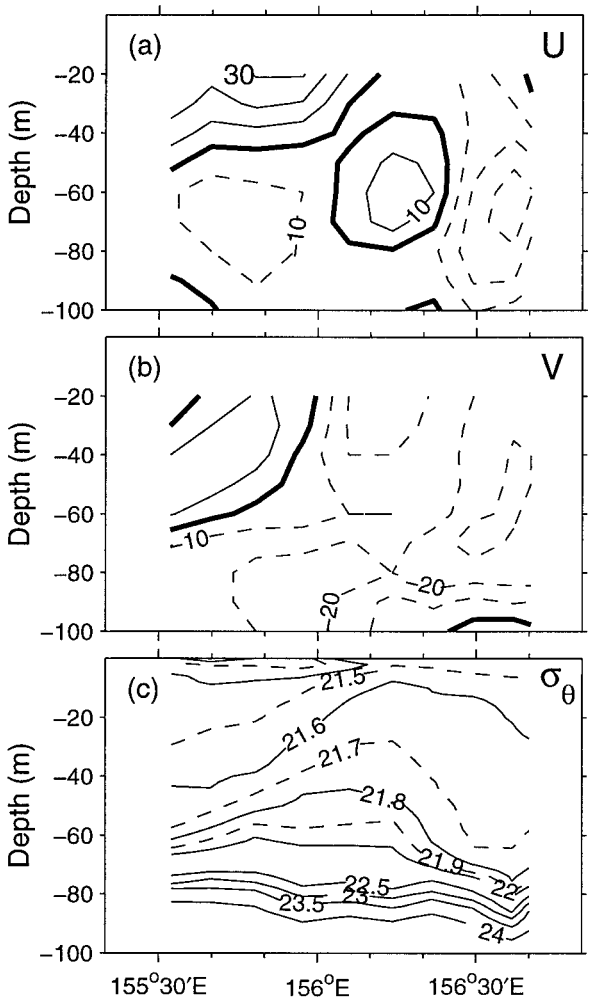

FIG. 5. (a) Zonal and (b) meridional current speeds (cm s^{-1}), and (c) potential density along the W2E section on 9 Jan denoted by the white triangle in Fig. 2.

Figure 6 shows a meridional section from *Le Noroit*, giving complete coverage of the southern portion of the eddy. This section was taken almost simultaneously with the N2S section of *Wecoma* on 8 January. Both the velocity and density structure looked similar to the *Wecoma* section in the region of overlap. We note that *Le Noroit* measured slightly smaller current velocity than *Wecoma*. The eddy seemed to be superimposed on a larger-scale meridional front, which was associated with a general eastward geostrophic current south and north of the eddy structure. The subsurface countercurrent below 80 m existed equatorward of the *Wecoma* survey domain.

4. Isopycnal fit

In order to quantify the eddy structure we fit the isopycnal depths from the *Wecoma* data with a Gaussian shape; that is

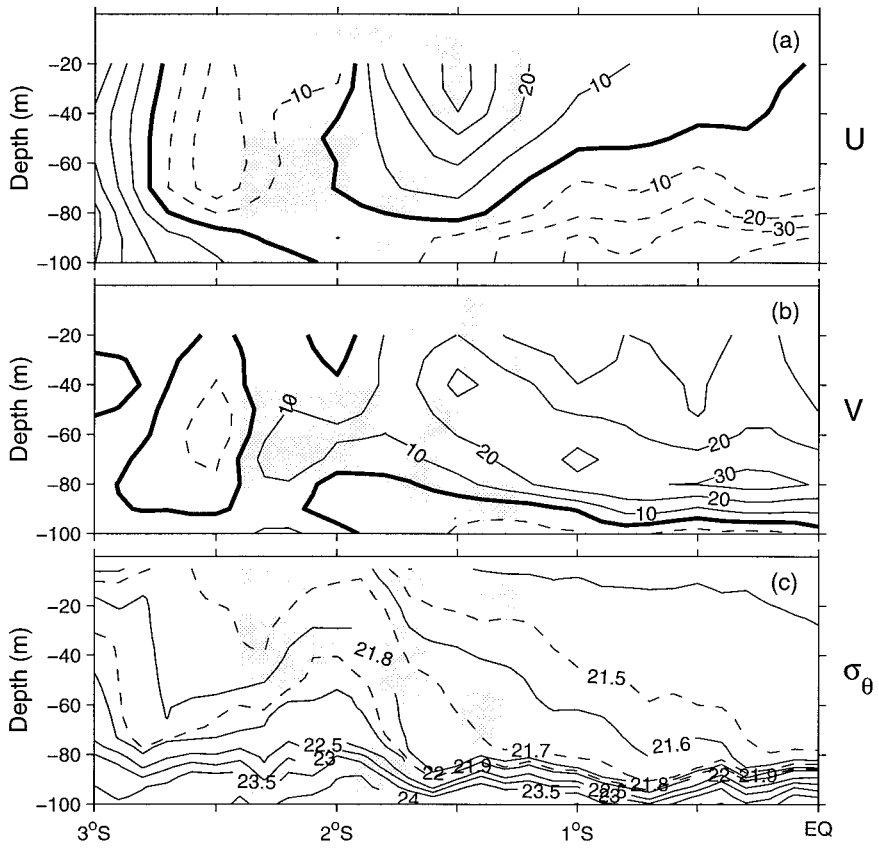

FIG. 6. (a) Zonal and (b) meridional current speeds (cm s^{-1}) and (c) potential density from the R/V *Le Noroit* N2S section on 8 Jan. The shaded areas denote the *Wecoma* survey domain.

$$h = h_0 + a_0 \exp\left[-\frac{(x - x_0)^2 + (y - y_0)^2}{r_0^2}\right], \quad (1)$$

where $h = h(x, y, t)$ is the depth of an isopycnal surface, h_0 is the background depth (i.e., the mean isopycnal depth in the absence of the eddy disturbance), (x_0, y_0) is the longitude and latitude of the eddy center, a_0 is the amplitude of the Gaussian, and r_0 is the e folding radius. We convert this into a linear regression problem to solve for a_0, x_0, y_0, and r_0 (see appendix). Approximately 3-day intervals (two circuits of the repeated survey) are used for each fit and a time series is obtained by moving the 3-day window forward one day at a time (Fig. 7).

The background depth (appendix) of the $\sigma_\theta = 21.7$ rises from about 90 m to 70 m (Fig. 7a), indicating the existence of upwelling in the thermocline. The radius from the fit decreases with time, from 120 km on 4 January to about 50 km when the eddy was well developed (Fig. 7d). Because the linear fit can only capture the upward domed structure of the isopycnals (appendix), the fits should capture the crest of the near-inertial gravity wave before the eddy was fully developed. Thus, the scale from the Gaussian fit can be used to represent the horizontal scale of the spindown of the surface jet. Note that the uncertainties of the eddy fit decrease with time. A simple spatial scale for the inertial motion on a β plane can be characterized as $(\beta t)^{-1}$ (D'Asaro 1989). Here, $\beta = 2.3 \times 10^{-11}$ s^{-1} m^{-1} is the meridional gradient of the Coriolis parameter, and t is the time, from 2 January, when the inertial motion was generated. The initial spatial scale of the inertial motion might be determined by the horizontal scale of the surface jet, while the trend of the radius decrease is consistent with $(\beta t)^{-1}$ (Fig. 7d).

The center point from the fit moves toward the northeast, at a mean speed of 9 and 15 cm s^{-1} in the zonal and meridional directions, respectively. This might be partly due to meridional propagation of the gravity wave (Eriksen 1993; 1999) and partly due to advection by the mean flow. Typically, the eddy fit explains 40%–80% of the variance of the isopycnal depth, which tends to increase with time. The fit centered on 6 January is less reliable because the fitted center is outside of the survey domain.

On 9 January when the eddy was well developed (the last fit in Fig. 7), the $\sigma_\theta = 21.7$ isopycnal background depth is 70 m, the center point of the eddy is at 2.1°S,

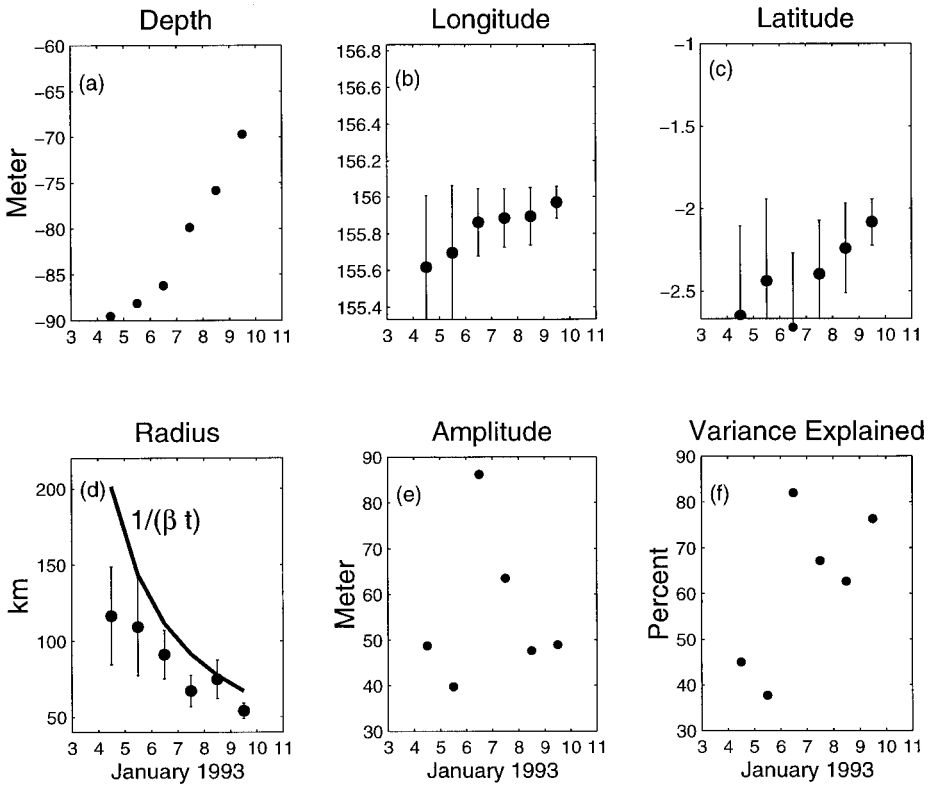

FIG. 7. (a) Background depth, (b) longitude, (c) latitude, (d) radius, (e) amplitude, and (f) explained variance from the Gaussian fit of the *Wecoma* 21.7σ_θ isopycnal using an approximate 3-day moving window. The vertical bars in (b), (c), and (d) denote standard errors of the estimates. The heavy line in (d) denotes the scale determined by $(\beta t)^{-1}$.

156°E, south-southwest of the butterfly crossover point, the radius is 53 km, and the amplitude is 49 m. These numbers are all in agreement with the eddy descriptions in the last section. From the bootstrap analysis (see appendix), the standard errors for center point longitude, latitude, and eddy radius are 10, 16, and 5 km, respectively, and the fit explains nearly 80% of the variance. When we fit the 0–80-m averaged dynamic height relative to 80 m (representative of the upper layer in a two-layer model) with a Gaussian shape using the above fixed center point and radius, the amplitude corresponds to a surface elevation of 1.2 cm (as a body force). So $g' = 2.4 \times 10^{-3}$ m s^{-2} is the reduced gravity of the two-layer model separated by the 21.7 σ_θ isopycnal used to describe the eddy (Gill 1982).

5. Eddy dynamics

In this section, we quantify several dynamical aspects of the eddy. First we analyze the dynamic balance of the leading terms within a cyclonic eddy to confirm the eddy structure. Then we discuss the relative vorticity evolution in the *Wecoma* survey domain and its relationship to the forcing terms. Finally, we discuss the potential vorticity, available potential energy, and kinetic energy of the eddy. From this analysis, we confirm that the development of the negative eddy vorticity is strongly related to the surface jet spindown processes, such as meridional inertial motion and surface layer convergence; the eddy appears to draw energy from the kinetic energy of the decaying jet.

a. Dynamic balance

A parameter describing an eddy on a β plane is $\epsilon = \beta L_R / f_0$, where $L_R = (g'\overline{h})^{1/2}/f_0$ is the local deformation radius (Killworth 1983). From the results of the previous section, $g' = 2.4 \times 10^{-3}$ m s^{-2} and $\overline{h}$ is set to be 50 m, the scale depth of wind forcing (Ralph et al. 1997) and also the approximate mean depth of the $\sigma_\theta = 21.7$ isopycnal in Fig. 4e. Thus, L_R is 70 km and $\epsilon = 0.3$. (The β drift velocity of the eddy, $\beta L_R^2/2$, is about 0.05 m s^{-1}.) Using the formula for the local deformation radius near the equator (Philander 1978) $L_R = c/(f_0 + \beta L_R)$, gives $L_R = 83$ km and a slightly higher ϵ. The L_R is smaller than the deformation radius for equatorial trapped waves, $(c/\beta)^{1/2} = 123$ km. Thus, ϵ can still be considered a small parameter so that we can expand the dynamic equations in terms of ϵ. The zero-order dynamic balance equation for a stationary cyclonic eddy in polar coordinates is

$$\frac{V^2}{r} + f_0 V = \frac{1}{\rho_0}\frac{\partial P}{\partial r}, \quad (2)$$

where r is the distance from the eddy center and V is the rotational velocity (Killworth 1983).

In order to evaluate the pressure gradient term for the N2S *Wecoma* section on 8 January, we linearly stretch the isopycnals between the sea surface and $\sigma_\theta = 22.5$ (whose mean depth is at 80 m) to 0–80 m (Fig. 8a). That is, the stretched coordinate at each station $\eta = z/z_r \times 80$ m, where $z_r = z|_{\sigma_\theta=22.5}$. This stretching reduces noise from the internal gravity waves, under the assumption that these waves have low wavenumbers and larger vertical scales (Godfrey et al. 1999). Also it eliminates the background slope contribution in the thermocline that is not related to the eddy. Similar stretching is applied to the velocity data, with no significant change to the velocity structure (Fig. 8b). Note that only the zonal component is used in the calculation by assuming that the section cuts through the eddy center, simplifying the calculation in light of availability of data.

The presure gradient relative to 80 m from the stretched density data for the N2S *Wecoma* section on 8 January is shown in Fig. 8c. The pressure gradient per unit mass at 20 m reaches 5×10^{-6} m s^{-2} at the northern limb of the eddy and 4×10^{-6} m s^{-2} in the south. The slight asymmetry may be due to the background gradient in the mixed layer, which cannot be completely removed by the above isopycnal stretching. The zero pressure gradient contour is located at 2°4′S near the surface and tilts southward with increasing depth to about 2°10′S at 80 m. The zero pressure gradient location is consistent with the eddy center from the isopycnal fit. The maximum pressure gradient is closer to the eddy center than the maximum velocity, and the Coriolis force only has a maximum magnitude of 2×10^{-6} m s^{-2} at 20 m (Fig. 8d) so that the pressure gradient is not fully balanced by the Coriolis force. It turns out that the centrifugal force (Fig. 8e) relative to the eddy center (using 2°6′S) is more important than the Coriolis force for balancing the pressure gradient force, consistent with the large Rossby number.

More details of the dynamic balance can be derived from the eddy fit. From the Gaussian fit of the 21.7 isopycnal, a peak tangential velocity of 0.3 m s^{-1} in the upper layer is obtained at 47 km from the center of the eddy as evaluated from Eq. (A2). The velocity fit with fixed eddy center and radius [Eq. (A3)] yields a similar velocity magnitude. This confirms the Gaussian shape and zero-order dynamic balance of the eddy. The $O(\epsilon)$ terms may be important to cause north–south asymmetry of the eddy (Killworth 1983); however, a detailed analysis of the $O(\epsilon)$ terms is beyond the scope of the present descriptive study.

b. Vorticity balance

The vertically integrated vorticity equation on a β plane is written as

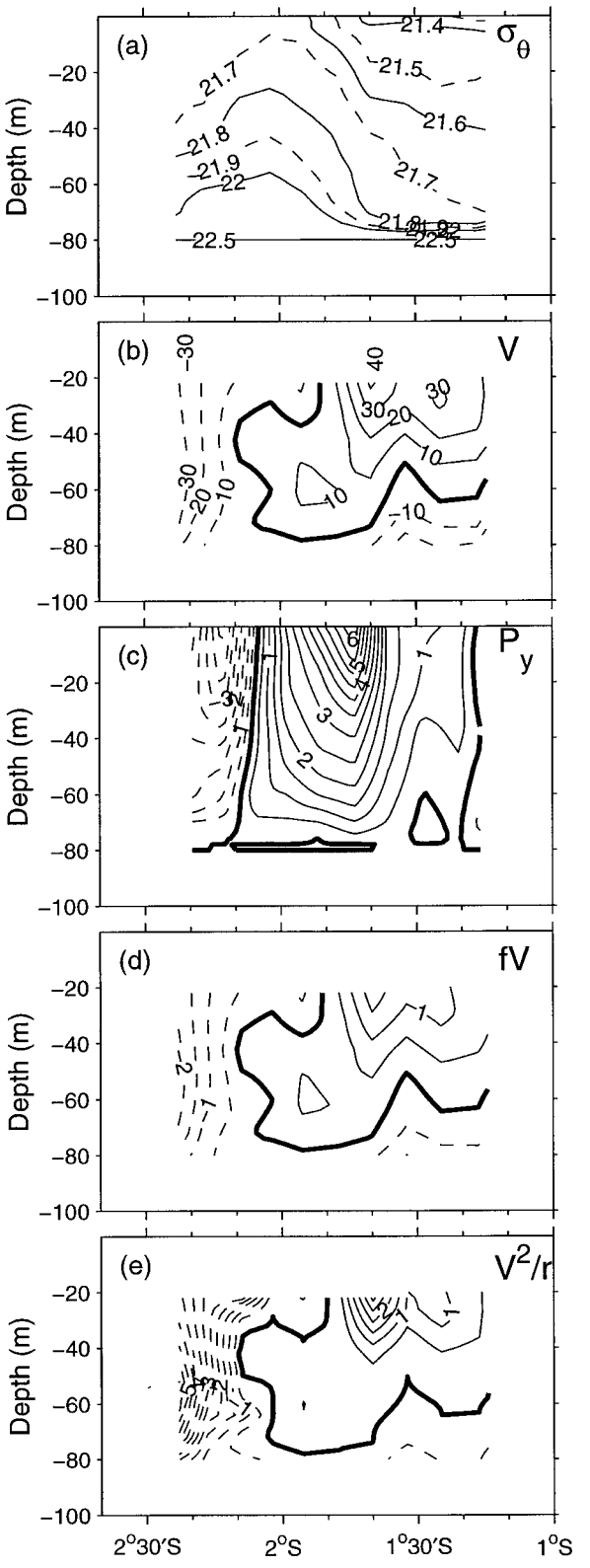

FIG. 8. (a) Stretched potential density, (b) stretched zonal velocity component (representing the rotational velocity V in cm s^{-1}), (c) pressure gradient force, (d) Coriolis force, and (e) centrifugal force from the N2S *Wecoma* section on 8 January. The units for (c), (d), and (e) are force per unit mass $\times 10^{-6}$ m s^{-2}.

$$\frac{\partial \xi}{\partial t} = -(f_0 + \xi)D - \beta v + \frac{\mathrm{curl}(\tau)}{\rho_0 H_0} + R, \qquad (3)$$

where $\xi = \partial v/\partial x - \partial u/\partial y$ and $D = \partial u/\partial x + \partial v/\partial y$ are the vertical mean relative vorticity and divergence in the upper 50 m. No velocity shear is assumed in the upper 20 m. Here τ is wind stress, H_0 is the mean layer thickness, set to 50 m, and

$$R = -\left[u\frac{\partial \xi}{\partial x} + v\frac{\partial \xi}{\partial y} + \frac{\partial}{\partial x}\left(w\frac{\partial v}{\partial z}\right) - \frac{\partial}{\partial y}\left(w\frac{\partial u}{\partial z}\right)\right] + \text{dissipation},$$

which includes terms that cannot be resolved by the survey data.

We fit $u[x(t), y(t), t] = \overline{u} + u_x x + u_y y + u_t t + u'[x(t), y(t), t]$ from the *Wecoma* data within 3-day intervals, where $u = u[x(t), y(t), t]$ is the variable to be fit; x and y are the longitude and latitude relative to the crossover point; t is the time relative to the center time of the interval; $\overline{u}$, u_x, u_y, and u_t are constants within that interval; and u' is the residual of the fit. In this sense, the $\overline{u}$ represents the mean value of u at the crossover point, u_x and u_y represent the mean zonal and meridional gradients, and u_t is mean rate of temporal change, during the 3-day time interval. In this way, the relative vorticity ξ and divergence of the velocity field D are calculated from linear fits of the *Wecoma* data within a 3-day moving window (Feng et al. 1998b). The vertical velocity w is calculated from the combination of the divergence field D and the density equation (Feng et al. 1998b). The vorticity and divergence calculated here represent the variability over the whole survey region. The wind stress curl is evaluated from daily NCEP reanalysis data.

Significant convergence exists in the surface layer due to the near-inertial motion of surface current, which lasts until the eddy is fully developed and is evidenced in the vertical velocity plot (Fig. 9a). The convergence stretches the surface layer and induces negative relative vorticity (Fig. 9b). Also, the northward advection after the WWB converts planetary vorticity to negative relative vorticity (Fig. 9b). The wind stress curl has little effect on the vorticity in the IFA region during this time period. Similar conclusions could be drawn for the *Wecoma* wind stress (not shown). The deep layer upwelling that occurs after 6 January may not be related to the surface process.

Figure 9c shows the evolution of vorticity at the center of the *Wecoma* Array. We see that the sum of the β effect and divergence terms steadily produce negative vorticity in the IFA, while substantial negative vorticity development related to the eddy only starts from 6 January. The discrepancy may be due to the inhomogeneity of the field or the unresolved vorticity advection effects. Overall, the vorticity source of the cyclonic eddy is primarily from the nonlinear term, that is, the surface layer convergence. This is also consistent with the decreasing spatial scale of the inertial motion, which increases the Rossby number and the nonlinearity of the decaying surface jet.

c. Eddy energetics

We first calculate the potential vorticity based on the 8 January N2S *Wecoma* section. The potential vorticity is defined as PV $\equiv (\partial\rho/\partial z)[(V/r) + (\partial V/\partial r) + f]$ (Kamenkovich et al. 1986). After the WWB diminishes, PV is a Lagrangian invariant if the remaining forcing and dissipation can be ignored. Between the 21.7 and 21.9 σ_θ, the PV isolines and isopycnals are almost parallel (Fig. 10a) so that there is not a PV barrier between the eddy and the surrounding water. The water exchange between the eddy and surrounding area could substantially affect the surface layer thermohaline structure. Strong turbulent dissipation rates were observed at the base of the mixed layer near the WHOI mooring during the eddy spinup (Smyth et al. 1996), which could be facilitated by the eddy formation.

The available potential energy [$gz(\rho - \overline{\rho})$, where $\overline{\rho}(z)$ is the potential density at the northernmost station, representing the background density] and kinetic energy [$\rho_0(u^2 + v^2)/2$] are calculated for the 8 January meridional section (Figs. 10b and 10c). Large available potential energy (>0.1 J kg^{-1}) is located near the center of the eddy above 40 m. Kinetic energy in the northern and southern limbs of the eddy is typically less than 0.1 J kg^{-1}. The mean kinetic energy averaged between 20 and 80 m is 2.9×10^{-2} J kg^{-1}, while the mean available potential energy between 20 and 80 m along the section is 4.1×10^{-2} J kg^{-1}, with a sum of 7.0×10^{-2} J kg^{-1}. Theoretically, the ratio between the potential energy and kinetic energy for the eddy is approximately $(r_0/L_R)^2$ (Gill 1982; r_0 is the eddy radius and L_R is the Rossby deformation radius), which is less than one in the present case. Thus, the larger potential energy here may be due to the selection of the background density profile complicated by the existence of the meridional density front.

A similar calculation is carried out for the meridional section on 7 January (Fig. 4d), when the mean kinetic energy along the section is 6.2×10^{-2} J kg^{-1} and the available potential energy is 3.7×10^{-2} J kg^{-1}, with a sum of 9.9×10^{-2} J kg^{-1}. If there are no other processes involved and the 20–80 m average is representative of the eddy, the kinetic energy loss between 7 and 8 January is 3.3×10^{-2} J kg^{-1} while the potential energy only slightly increases by 0.4×10^{-2} J kg^{-1}, which means that part of the decaying jet kinetic energy is converted to eddy kinetic energy and eddy potential energy during the eddy spinup. The difference of the mean total energy between the two sections is 2.9×10^{-2} J kg^{-1}, or about 30% of the total near-inertial energy, which may be carried away by vertically propagating near-inertial gravity waves or partly dissipated.

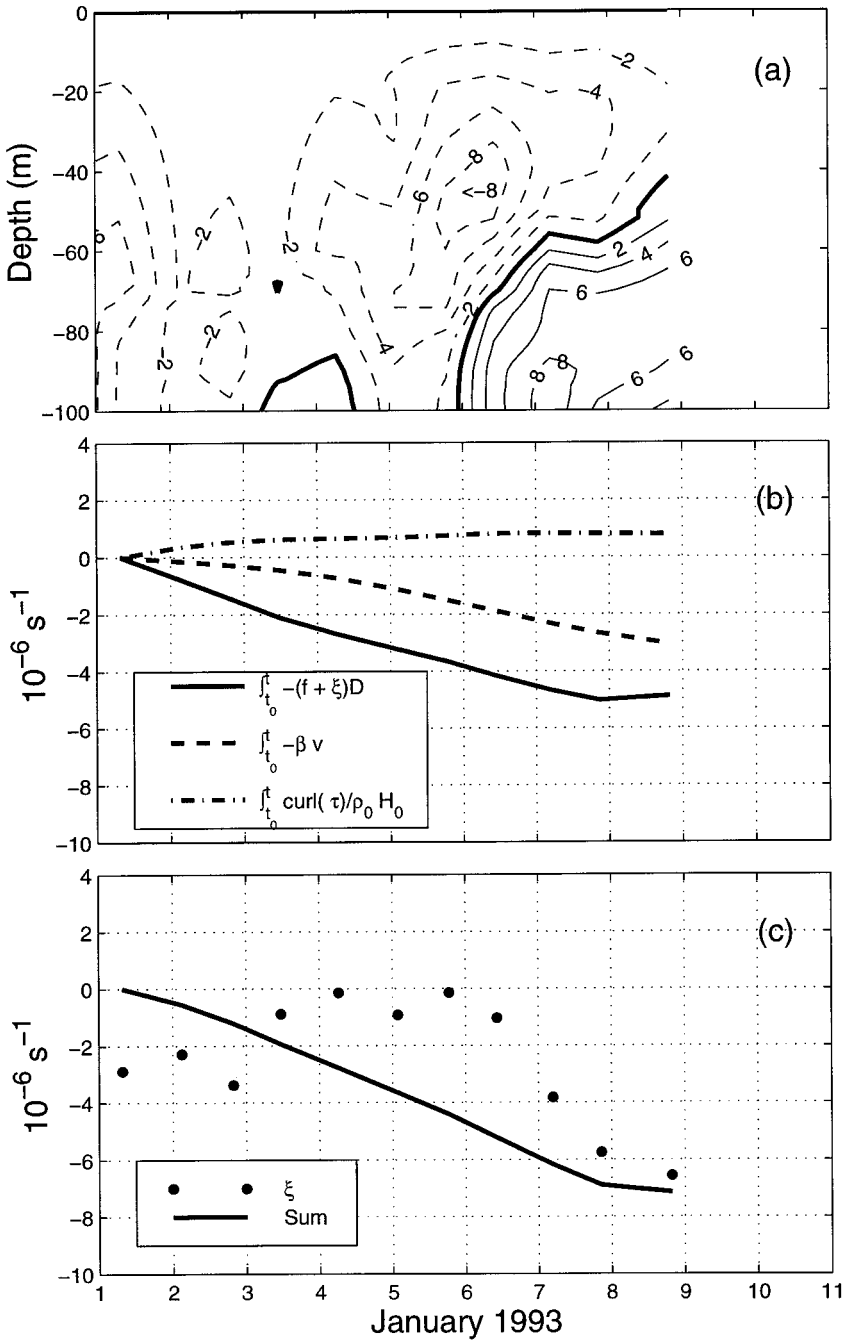

FIG. 9. (a) Vertical velocity and (b) cumulative vorticity forcing terms acting on 0–50 m; (c) comparison between vorticity evolution averaged between 0 and 50 m and the sum of the forcing terms in (b). The units for vertical velocity are meters per day. Positive vertical velocity is upward.

The analysis above indicates that the spindown of the eastward surface jet in the near-equatorial region is unstable; that is, smaller scale variability is generated during this process. Also the eddy field appears to draw energy from the mean flow kinetic energy. In general it may be regarded as a barotropic instability process.

6. Discussion and summary

In the present study, we described the spinup of a submesoscale cyclonic eddy during the spindown of the intense eastward surface jet forced by the December 1992–January 1993 WWB using the R/V *Wecoma* re-

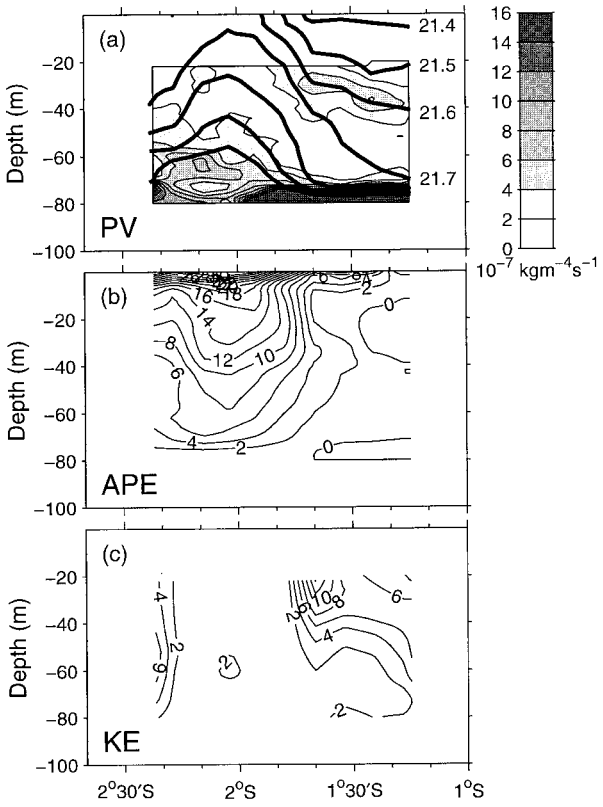

FIG. 10. (a) Potential vorticity, (b) available potential energy, and (c) kinetic energy from the N2S *Wecoma* section on 8 Jan. The contour superimposed in (a) is the potential density as shown in Fig. 8a. Units of APE and KE are 10^{-2} J kg^{-1}.

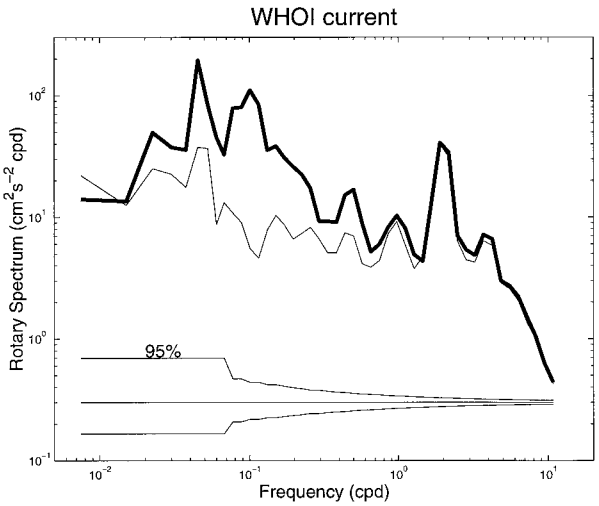

FIG. 11. Mean rotary spectrum of upper 100-m WHOI velocity. The bold line denotes the anticyclonic component and the thin line is the cyclonic component. The 95% confidence interval is shown.

peated survey velocity and potential density data during the TOGA COARE IOP. The surface jet attained a speed of 0.6 m s^{-1} in the survey region centered at 1.8°S. When the wind burst relaxed from 2 January 1993, the surface jet started to decay and inertial motion was generated. The submesoscale cyclonic eddy was spun up on 8 January, within half an inertial period.

A Gaussian shape was fit to the 21.7 σ_θ isopycnal from the repeated survey data, determining the eddy center to be south-southwest of the crossover point of the survey pattern. The radius was about 50 km, smaller than the local Rossby radius of deformation. A dynamic analysis confirms that the zeroth-order balance within the eddy is $V^2/r + f_0 V = \rho_0^{-1}\partial P/\partial r$. From the vorticity analysis, surface layer convergence related to the surface jet and northward advection during the spindown of the surface jet were found to cause the negative eddy vorticity, with the nonlinear convergence term being dominant. The eddy appeared to draw energy from the mean flow kinetic energy.

A novel result of the present study is that the horizontal scale of the inertial motion in the near-equatorial region is strongly influenced by the β effect. That is, the decaying surface jet had decreasing horizontal scale with time, $(\beta t)^{-1}$. Due to the small Coriolis parameter near the equator, $(\beta t)^{-1}$ determines the spindown spatial scale of the inertial motion, and the decreased spatial scale makes it possible to generate the highly nonlinear submesoscale eddy. This eddy may have had an impact on the heat, salt, and momentum balance of the upper ocean in response to the WWB.

Figure 11 shows the rotary velocity power spectrum from the WHOI mooring, averaged over the upper 100 m. There are prominent oscillations at the 6-h, semidiurnal, diurnal, and 2-day periods. In the low-frequency portion of the spectrum, the largest ratio between the anticyclonic and cyclonic energy is in the 10–13-day time period, indicating dominance of near-inertial gravity wave activity within its critical latitude. There is also another peak near 20 days. Helber and Weisberg (1998) concluded that 14–23-day oscillations near the equator at this longitude were dominated by downward propagating Rossby–gravity waves, which also had a dominant anticyclonic rotation. From a wavelet analysis (not shown), the upper-ocean motion is dominated by near-inertial motion (and the 20-day mixed Rossby–gravity wave is absent) during late December 1992 to early January 1993.

As pointed out in Section 4, the near-inertial gravity wave on a β plane has a decaying horizontal spatial scale with time, $(\beta t)^{-1}$ (D'Asaro 1989). This was also evidenced in a linear analytical model of the wind-driven response of the upper equatorial ocean (Eriksen 1993), and the linear assumption broke down only a few days after onset of the wind burst with an assumed mixed layer depth of 30 m. Eriksen argued that by setting the mixed layer depth to 100 m, the occurrence of the nonlinearity could be delayed. However, even during the strongest December 1992 wind burst, the mixed layer depth never surpassed 70 m (Smyth et al. 1996). Alternatively, he suggested that vertical mixing neglect-

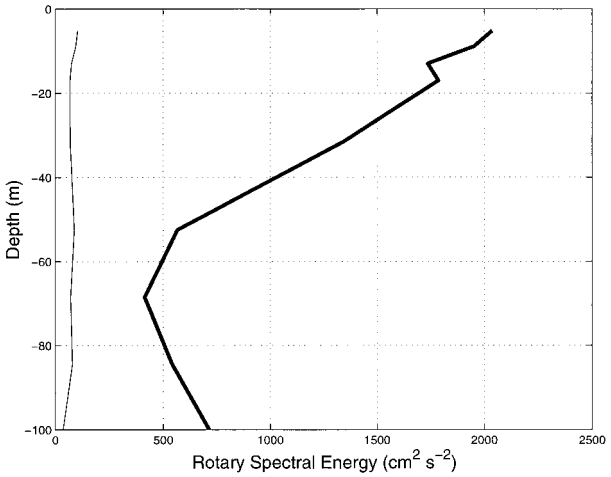

FIG. 12. Mean rotary spectrum of upper 100 m WHOI velocity for the 10–13-day period band. Line types are as for Fig. 11.

ed in the linear model might hamper the development of the nonlinearity. There are two competing factors that affect the Rossby number, Ro $= U/f_0L$. Either increasing the mixed layer depth or the vertical mixing reduces the magnitude of U, the horizontal velocity, and thus reduces the Rossby number. On the other hand, the horizontal scale L set by the β effect decreases with time, increasing the Rossby number. The scale of the inertial motion may also be affected by the the scale of the wind field and its translation speed (D'Asaro 1989).

Generation of the nonlinearity from the inertial motion may also depend on other factors, which requires additional theoretical work and numerical modeling. From these observations, the direct response of the upper ocean to the wind burst was the generation of the Yoshida jet, and the inertial motion seemed to be generated during the decay phase of the surface jet. Smyth et al. (1996) found that the oscillatory wake left by a previous westerly wind event could affect the surface current response to the instantaneous wind stress during this WWB peak. Thus, the surface jet during our study period may have been amplified and prolonged by previous westerly peaks, and the spindown process could also be affected by the wind stress history.

Vertical propagation of the near-inertial energy seems to be ineffective in removing the energy from the surface layer. From the vertical structure of the near-inertial energy, it seems that most of the energy is trapped in the upper 50 m (Fig. 12). Eriksen (1999) found that near-inertial motions at several frequencies had consistent vertical propagation structure. The selectiveness of vertical propagation of internal waves at different frequencies has been addressed using vertical propagating modes (Philander 1978). Presumably, the strong pycnocline due to both temperature and salinity stratification could hamper the downward propagation of the near-inertial energy. A similar conclusion was drawn from a much shorter time series during COARE by Smyth et al. (1996).

Our analysis of this submesoscale eddy suggests the importance of the nonlinear terms in the upper-ocean momentum balance in the near-equatorial western Pacific warm pool during the spindown of the strong eastward surface jet. Without further observations, it is impossible to determine the net impact of such eddies on the long-term heat, salt, and momentum budgets of the warm pool, though the impact may be quite large during brief intervals. Models that incorporate the necessary physics and resolution may be useful for making an estimation. The relative frequency and spatial distribution of such eddies must also be determined in order to estimate their integral impact. Right now, we have no information about the frequency of occurrence of such eddies. In the warm pool region, they are likely to be important only in conjunction with the WWB-driven eastward jets.

Acknowledgments. PH and RL were supported by NSF Grant OCE-9525986. MF was supported by the International Pacific Research Center at the University of Hawaii and by CSIRO Marine Research. We thank Dail Rowe and two reviewers for helpful suggestions. R/V *Le Noroit* data were provided by G. Eldin and K. Richards. Jeff Dunn makes the NCEP data easily accessible.

APPENDIX

Isopycnal Fit

Because the Gaussian distribution is not linear and the results of nonlinear regression depend on the specified initial condition, we linearize the fitting problem of Eq. (1). For an isopycnal surface depth $h = h[x(t), y(t), t]$ (positive upward), we first remove a temporal trend and 10% of the deepest isopycnal depth points to stabilize the fit. Then we find the deepest depth in the remaining data, $h_{\min}$, use $h_0 = h_{\min} - 1$ (m) as the background depth (ensuring the following conversion to be finite), and convert h to $h_1 = \log(h - h_0)$. We fit h_1 with

$$h_1 = c_1(x^2 + y^2) + c_2x + c_3y + c_4, \qquad \text{(A1)}$$

where $c_1 = -1/r_0^2$, $c_2 = 2x_0/r_0^2$, $c_3 = 2y_0/r_0^2$, and $c_4 = \log(a_0) - (x_0^2 + y_0^2)/r_0^2$. Thus, $r_0 = (-1/c_1)^{1/2}$, $x_0 = 2r_0^2c_2$, $y_0 = 2r_0^2c_3$, and $a_0 = \exp[c_4 + (x_0^2 + y_0^2)/r_0^2]$. We use a bootstrap method to calculate the standard errors of the coefficients c_n (Efron and Tibshirani 1986). Then, we use linear relations to calculate the standard errors in r_0, x_0, and y_0.

From the zeroth-order eddy dynamic balance of Eq. (3), we calculate the tangential velocity of the eddy based on the pressure disturbance; that is,

$$V = [-fr + fr(1 + 4P_r/\rho_0f^2r)^{1/2}]/2.$$

Assuming that P has a Gaussian shape, that is, $P_r/\rho_0 = -g'h_r$, where $h_r = -2a_0 r/r_0^2 \exp(-r^2/r_0^2)$, we have

$$V = \frac{-fr + fr[1 + 8a_0 g'/f^2 r_0^2 \exp(-r^2/r_0^2)]^{1/2}}{2}. \quad \text{(A2)}$$

On the other hand, knowing the center and radius of the eddy, we can obtain the eddy magnitude, a_0, from linear fit of the velocity data; that is,

$$8a_0 g' r^2/r_0^2 \exp(-r^2/r_0^2) = 4frV + 4V^2. \quad \text{(A3)}$$

REFERENCES

D'Asaro, E. A., 1989: The decay of wind-forced mixed layer inertial oscillations due to the β effect. *J. Geophys. Res.*, **94,** 2045–2056.

Efron, B., and R. J. Tibshirani, 1986: Bootstrap methods for standard errors, confidence intervals and other measures of statistical accuracy. *Stat. Sci.,* **1,** 54–77.

Eldin, G., T. Delcroix, C. Henin, K. Richards, Y. du Penhoat, J. Picaut, and P. Rual, 1994: Large-scale current and thermohaline structures along 156°E during the COARE Intensive Observation Period. *Geophys. Res. Lett.,* **21,** 2681–2684.

Eriksen, C. C., 1993: Equatorial ocean response to rapidly translating wind bursts. *J. Phys. Oceanogr.,* **23,** 1208–1230.

——, 1999: Observations of low-latitude, near-inertial waves forced by westerly wind bursts. *Proc. 'Aha Huliko'a: Hawaiian Winter Workshop,* Honolulu, HI, University of Hawaii at Manoa, 173–179.

Feng, M., M. Merrifield, R. Pinkel, P. Hacker, A. Pluddemann, E. Firing, R. Lukas, and C. Eriksen, 1998a: Semidiurnal tides observed in the western equatorial Pacific during TOGA COARE. *J. Geophys. Res.*, **103,** 10 253–10 272.

——, P. Hacker, and R. Lukas, 1998b: Upper ocean heat and salt balances in response to a westerly wind burst in the western equatorial Pacific during TOGA COARE. *J. Geophys. Res.*, **103,** 10 289–10 311.

——, R. Lukas, P. Hacker, R. Weller, and S. Anderson, 2000: Upper ocean heat and salt balances in the western Pacific in response to the intraseasonal oscillation during TOGA COARE. *J. Climate,* **13,** 2409–2427.

Gill, A. E., 1982: *Atmosphere–Ocean Dynamics.* Academic Press, 662 pp.

Godfrey, J. S., E. F. Bradley, P. A. Coppin, L. F. Pender, T. J. McDougall, E. W. Schulz, and I. Helmond, 1999: Measurements of upper ocean heat and freshwater budgets near a drifting buoy in the equatorial Indian Ocean. *J. Geophys. Res.,* **104** (C6), 13 269–13 302.

Helber, R. W., and R. H. Weisberg, 1999: Wave kinematics in the western Pacific warm pool: The period band from 14 to 23 days. *Proc. Conf. on the TOGA Coupled Ocean–Atmosphere Response Experiment (COARE),* Boulder, CO, World Climate Research Programme Tech. Doc. WCRP-107, 295–296.

Huyer, A., P. M. Kosro, R. Lukas, and P. Hacker, 1997: Upper-ocean thermohaline fields near 2°S, 156°E during TOGA-COARE, November 1992 to February 1993. *J. Geophys. Res.,* **102,** 12 749–12 784.

Kamenkovich, V. M., M. N. Koshlyakov, and A. S. Monin, 1986: *Synoptic Eddies in the Ocean.* D. Reidel, 433 pp.

Killworth, P. D., 1983: On the motion of isolated lenses on a beta-plane. *J. Phys. Oceanogr.,* **13,** 368–376.

Lukas, R., P. Hacker, M. Mao, E. Firing, A. Huyer, and P. M. Kosro, 1995: Upper ocean currents in the Intensive Flux Array during TOGA COARE. *Proc. TOGA'95,* Melbourne, Australia, WCRP-91, WMO/TD 717, 542–546.

Philander, S. G. H., 1978: Forced oceanic waves. *Rev. Geophys. Space Phys.* **16,** 15–46.

Ralph, E. A., K. Bi, P. P. Niiler, and Y. du Penhoat, 1997: A Lagrangian description of the western equatorial Pacific response to the wind burst of December 1992: Heat advection in the warm pool. *J. Climate,* **10,** 1706–1721.

Richardson, R., I. Ginis, and L. Rothstein, 1999: A numerical investigation of the local ocean response to westerly wind burst forcing in the western equatorial Pacific. *J. Phys. Oceanogr.,* **29,** 1334–1352.

Schureman, P., 1958: Manual of harmonic analysis and prediction of tides. Special Publ., 98, U.S. Govt. Printing Office, Washington, DC, 317 pp.

Smyth, W. D., D. Hebert, and J. N. Moum, 1996: Local ocean response to a multiphase westerly wind burst. Part 1: Dynamic response. *J. Geophys. Res.,* **101,** 22 495–22 512.

Soloviev, A., R. Lukas, and P. Hacker, 2000: Horizontal structure of the upper ocean velocity and density fields in the western equatorial Pacific warm pool: Depth range from 20 to 250 m. *J. Phys. Oceanogr.,* **30,** 416–432.

Webster, P. J., and R. Lukas, 1992: TOGA COARE: The Coupled Ocean-Atmosphere Response Experiment. *Bull. Amer. Meteor. Soc.,* **73,** 1377–1415.

Weller, R. A., and S. P. Anderson, 1996: Surface meteorology and air–sea fluxes in the western equatorial Pacific warm pool during the TOGA Coupled Ocean–Atmosphere Response Experiment. *J. Climate,* **9,** 1959–1990.

Zhang, Q., and L. Rothstein, 1998: Modeling the oceanic response to westerly wind bursts in the western equatorial Pacific. *J. Phys. Oceanogr.,* **28,** 2227–2249.